Geophysical Journal International

Geophys. J. Int. (2020) **221,** 2091–2103
GJI Rock and Mineral Physics, Rheology

doi: 10.1093/gji/ggaa130

Relating strain localization and Kaiser effect to yield surface evolution in brittle rocks

Hannah Gajst,[1,2] Eyal Shalev,[2] Ram Weinberger,[2,3] Shmuel Marco,[1] Wenlu Zh[4] and Vladimir Lyakhovsky[2]

[1] *The Department of Geophysics, Tel-Aviv University, Tel-Aviv* 69978, *Israel. E-mail: gajsthannah@mail.tau.ac.il*
[2] *Geological Survey of Israel,* 32 *Yesha'ayahu Leibowitz, Jerusalem* 9371234, *Israel*
[3] *Department of Geological and Environmental Science, Ben Gurion University of the Negev, Beer Sheva* 84105, *Israel*
[4] *Department of Geology, University of Maryland,* 237 *Regents Drive, College Park, MD* 20742, *USA*

Accepted 2020 March 8. Received 2020 March 8; in original form 2019 August 20

SUMMARY

The yield surfaces of rocks keep evolving beyond the initial yield stress owing to the damage accumulation and porosity change during brittle deformation. Using a poroelastic damage rheology model, we demonstrate that the measure of coupling between the yield surface change and accumulated damage is correlated with strain localization and the Kaiser effect. Constant or minor yield surface change is associated with strong strain localization, as seen in low-porosity crystalline rocks. In contrast, strong coupling between damage growth and the yield surface leads to distributed deformation, as seen in high-porosity rocks. Assuming that during brittle deformation damage occurs primarily in the form of microcracks, we propose that the measured acoustic emission (AE) in rock samples correlates with the damage accumulation. This allows quantifying the Kaiser effect under cyclic loading by matching between the onset of AE and the onset of damage growth. The ratio of the stress at the onset of AE to the peak stress of the previous loading cycle, or Felicity Ratio (FR), is calculated for different model parameters. The results of the simulation show that FR gradually decreases in the case of weak coupling between yield surface and damage growth. For a strong damage-related coupling promoting significant yield surface change, the FR remains close to one and decreases only towards the failure. The model predicts that a steep decrease in FR is associated with a transition between distributed and localized modes of failure. By linking the evolving yield surface to strain localization patterns and the Kaiser effect, the poroelastic damage rheology model provides a new quantitative tool to study failure modes of brittle rocks.

Key words: Fracture and flow; Numerical approximations and analysis; Numerical modelling.

1 INTRODUCTION

1.1 Pre-failure damage localization patterns

Brittle failure controls the stability of rock mass and produces rock damage. The process of brittle failure is different for low-porosity crystalline (e.g. granite, $\phi < 1\%$) and high-porosity granular (e.g. sandstone, $\phi > 15\%$) rocks. While the former tends to form highly localized discrete slip surfaces, the latter may develop tabular zones of deformation bands prior to the formation of slip surfaces (Fig. 1). Both field and laboratory studies support this observation (e.g. Aydin & Johnson 1983; Lockner *et al.* 1992; Antonellini *et al.* 1994; Weinberger *et al.* 1995; Mair *et al.* 2000; Fossen *et al.* 2007; Gajst *et al.* 2018).

Failure of crystalline rock is often described, on multiple scales, as a localization process resulting in a discrete fault plane (e.g. Ben-Zion & Sammis 2003). An example of localization on a plate boundary scale of kilometres was discussed by Marco (2007), who demonstrated the gradual localization process of the Dead Sea Fault Zone into a single shear zone over millions of years, under a relatively constant regional stress field. In contrast, fault zones in porous sandstone are known to form packages of deformation bands, each accumulating a small amount of displacement (mm–cm). These zones can accumulate strains on the scale of up to several decimetres prior to the formation of a slip surface (Aydin & Johnson 1983; Antonellini *et al.* 1994; Fossen *et al.* 2007), suggesting repeated phases of localization and delocalization preceding faulting. Shipton & Cowie (2001) and Bernard *et al.* (2002) demonstrated that the

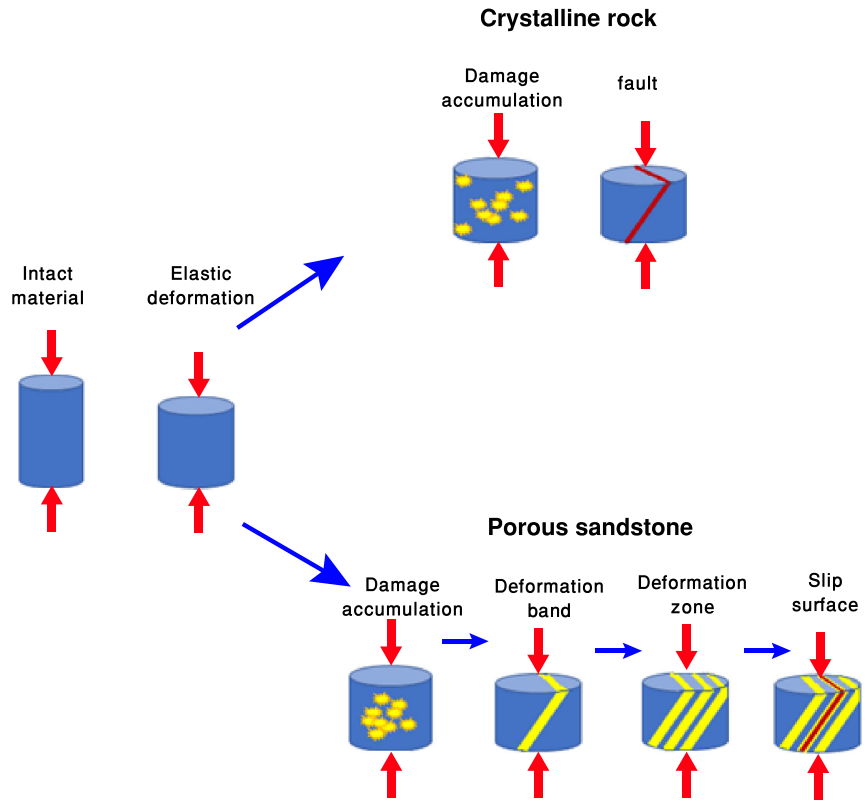

Figure 1. A schematic drawing of the damage accumulation stages in crystalline rocks and porous sandstones. Crystalline rocks show strong damage localization, while porous sandstone may experience several localization cycles in the form of multiple deformation bands forming prior to the development of a slip surface (i.e. fault).

zone of shear bands could continue to grow even after the formation of a slip surface, thus exhibiting distributed strain accumulation after faulting.

In the laboratory, acoustic emission (AE) is measured to probe microcracking during brittle deformation. Lockner *et al.* (1992) recorded locations of AE activities during fault propagation in axially loaded Westerly granite samples. Their results show that after an initial 'ringing phase', where AE was recorded throughout the sample, a fast localization process occurred. This coincided with the development of a localized fault zone and failure. In the same study, when subjected to similar experimental conditions, Weber sandstone samples underwent a slow transition from tabular distributed zones of AE activity to a localized planer zone of AE activity (Lockner *et al.* 1992). The sandstone samples did not exhibit an initial ringing phase, and their final deformation zones were thicker than those of the granite samples. Results of experiments of Locharbriggs sandstone (Mair *et al.* 2000) demonstrated the gradual formation of a package of shear bands clearly relating the amount of deformation and the number of strands (i.e. bands). They suggested that each strand accumulates a finite amount of strain before a new strand is formed. This can be interpreted as multiple transitions between modes of localized and distributed damage accumulation. The transition mechanism is difficult to explain since no evidence of strain hardening was observed in this experiment.

1.2 The Kaiser effect

The Kaiser effect (Kaiser 1953) is observed in rocks and materials subjected to repeated cycles of loading and unloading, where the peak stress increases from cycle to cycle. As long as the stress remains below the largest previously attained stress, the AE counts remain at zero or close to the background level. When reaching the previous peak stress, the system experiences a surge of AE activity (Kurita & Fujii 1979; Li & Nordlund 1993; Pestman & Munster 1996; Lavrov 2001). The Kaiser effect has been observed in a broad range of rocks and materials, including granite (Kurita & Fujii 1979; Li & Nordlund 1993), andesite (Yoshikawa & Mogi 1981), marble (Holcomb 1993a; Li & Nordlund 1993; Tuncay & Ulusay 2008), gneiss (Li & Nordlund 1993), sandstone (Kaiser 1953; Goodman 1963; Tuncay & Ulusay 2008), limestone (Lavrov 2001) and tuff (Tuncay & Ulusay 2008). The quality of the Kaiser effect is characterized by the Felicity Ratio (FR), which is the ratio of the stress (σ_{AE}) at the onset of AE to the peak stress (σ_{Max}) of the previous loading cycle. In the ideal case FR $= \sigma_{AE}/\sigma_{Max} = 1$, but in many cases it decreases during the experiment, as shown in Fig. 2 with data from Li & Nordlund (1993). When the stress during the cycle approaches the rock strength, the Kaiser effect deteriorates, and the FR steeply decreases. This tendency is reproduced by the model (coloured lines, also shown in Fig. 2), which is presented below.

The Kaiser effect is less pronounced when rocks are subjected to high shear deformation leading to dilation (Kurita & Fujii 1979). The FR values are affected by changing the strain rate between cycles (Lavrov 2001; Zhang *et al.* 2018), as well as the temperature (Li & Nordlund 1993). There have also been examples of sensitivity to healing processes (Lavrov 2003).

There is a general agreement that the Kaiser effect is connected to damage accumulation (e.g. Holcomb 1993b; Lavrov 2003; Hamiel *et al.* 2004a), yet there is no general model explaining the difference

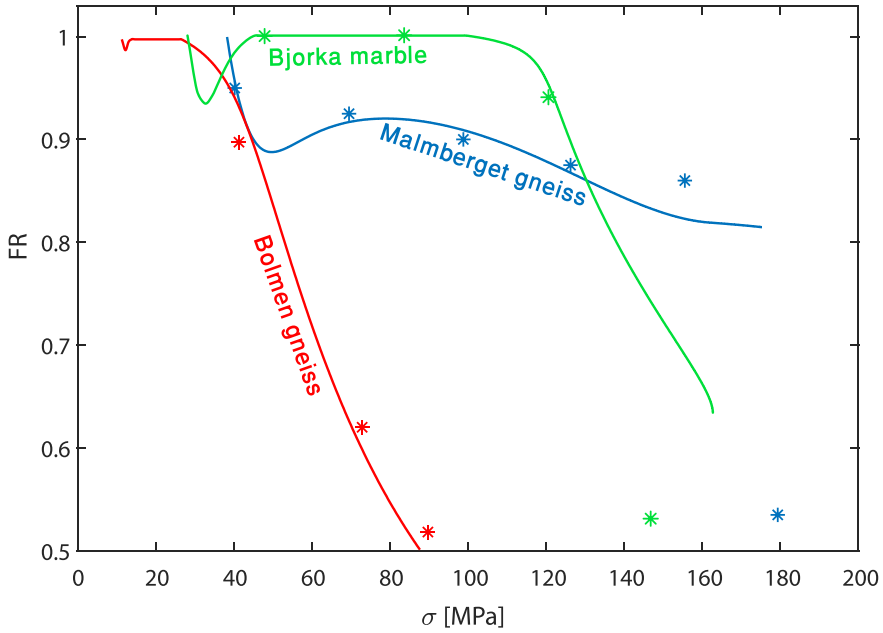

Figure 2. Felicity Ratio (FR) versus stress for three different types of rocks (marked with different coloured stars) obtained in the experiment of Li & Nordlund (1993). Lines with the same colours represent simulated FR of this study.

in the FR trends for various rock types, as well as second-order effects, such as time and strain rate sensitivity. A better understanding of the Kaiser effect and its sensitivities, especially in relation to localization processes, may help to predict failure on different scales.

1.3 Damage rheology modelling

Numerous experiments demonstrate that the yield surface of porous sandstones forms a cap-shaped line (e.g. Baud *et al.* 2006; Tembe *et al.* 2007). The 'yield cap' may be defined in notations of stresses or strains; its shape along, with the deformation path defines the mode of failure (e.g. Baud *et al.* 2004). Laboratory experiments of porous rocks show evidence of overall strain hardening and yield cap growth attributed to plasticity and porosity loss (e.g. Baud *et al.* 2006; Tembe *et al.* 2007 ; Bedford *et al.* 2018, 2019). Several mechanical 'yield cap' model formulations address the deformational processes in porous rocks. Elastoplastic formulation, also known as bifurcation analysis (e.g. Rudnicki & Rice 1975; Issen & Rudnicki 2000; Olsson & Holcomb 2000; Schultz & Siddharthan 2005), successfully predicts the orientation of deformation bands (sheer bands) but lacks any time dependency and temporal evolution of the bands. Continuum breakage models for mechanics of granular media accurately predict the yield surface and localization patterns of porous sandstones based on grain and cement properties (Das *et al.* 2014; Tengattini *et al.* 2014). Grueschow & Rudnicki (2005) discussed different models of evolving yield cap (DiMaggio & Sandler 1971; Carroll 1991) and developed a constitutive model connecting the yield cap growth with different failure modes. Results of numerical simulations utilizing different formulations incorporating changes of the local elastic properties and porosity-induced yield cap change explicitly, connecting different deformation patterns and modes of failure with the yield cap growth (e.g. Vorobiev *et al.* 2007; Stefanov *et al.* 2011; Lyakhovsky *et al.* 2015).

The yield surface for crystalline and low-porosity rocks are often approximated by a straight line representing the Coulomb failure criterion, yet the failure envelope of most rock types appears to curve with growing compression and confining pressure (Jaeger *et al.* 2007). Observed Kaiser effect in crystalline rock samples indicates strain hardening in consecutive cycles and is attributed to the change in the yield surface due to damage accumulation (Holcomb 1993b; Hamiel *et al.* 2004a).

In order to connect between localized and distributed damage accumulation during pre-faulting processes, yield surface evolution, and the Kaiser effect, we outline a new damage-rheology model formulation with an evolving damage-dependent yield surface. We use a semi-analytical approach and set of 1-D numerical simulations, which explain damage accumulation patterns and connects them to the felicity ratio of the Kaiser effect. We demonstrate that the model with a damage-dependent yield surface not only capable of reproducing the Kaiser effect but also connects the change in FR with transitions between two modes of brittle deformation, localized versus distributed fracturing, under low confining pressures.

2 METHODS

2.1 Model description

In this study, we follow the main derivations of the damage poroelastic model by Hamiel *et al.* (2004b) and Lyakhovsky *et al.* (2015) considering two thermodynamic state variables, porosity, ϕ, and damage, α, coupled by kinetic relations. The porosity refers to the volume fraction of pores with complete unloading. With this definition, the porosity can only change with inelastic deformation. The damage ranges between 0 and 1 ($\alpha = 0$ for intact material, and $\alpha \rightarrow 1$ for total failure) and is responsible for the rock stiffness and its degradation induced by microcracks, voids, or any other type of flaws. The key thermodynamic relations are briefly discussed in the Appendix. The detailed derivations and numerical results can be found in Lyakhovsky *et al.* (2015). They demonstrated that at the intermediate and high confining pressures, competition between inelastic compaction (porosity decrease) and dilation (porosity increase), damage accumulation, and healing leads to different modes

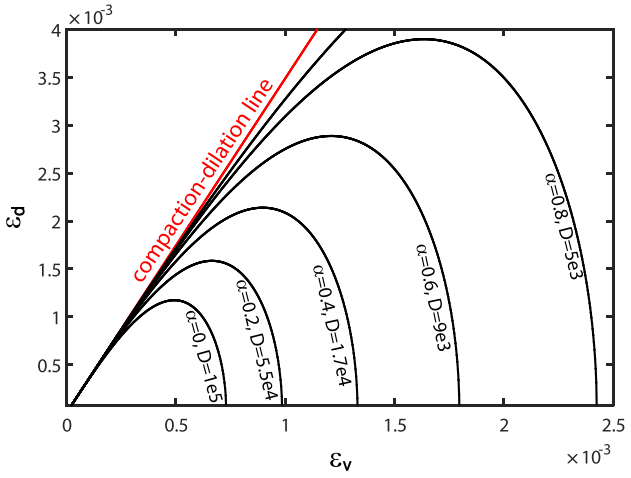

Figure 3. Yield surface change in strain coordinates as a function of damage. ε_v, ε_d are volumetric and differential strain components, respectively, yield cap growth parameter is $D_2 = -3$ and the power law is $n = 2$.

of failure in porous rocks. Incorporating porosity-dependent yield surface change allowed to successfully reproduce cataclastic flow with no significant localization in porous rocks at high confining pressures (above 170 MPa) and localized brittle failure at intermediate confining pressures (below 90 MPa).

In this study, we focus on the damage accumulation processes in the compaction regime under uniaxial unconfined conditions and, therefore, neglect the healing processes. Also, considering drained conditions or dry rocks, fluid pressure should be excluded. Very small porosity changes have a minor effect on the stress–strain relations and are also neglected. The crucial modification of the Lyakhovsky *et al.* (2015) model is the assumption that the model parameter, controlling the size of the yield surface depends not only on the porosity but also on the damage variable. Fig. 3 shows a series of yield surfaces for different damage values and one of the specified sets of the model parameters connecting damage with the D-value in eq. (4) (see the Appendix). A decrease in the D-value leads to a self-similar increase of the yield surface.

2.2 Model formulation

We consider 1-D uniaxial compression with all the model variables, displacement $u(x, t)$, strain $\varepsilon(x, t) = \partial u/\partial x$ (negative strain values stand for compaction), and damage $\alpha(x, t)$, depending only on the x coordinate and time t. Under these conditions, the 1-D damage kinetic equation (eq. A5 from the Appendix) is

$$\frac{d\alpha}{dt} = C_d \left[D(\alpha)(-\varepsilon)^{n+2} + \varepsilon^2 (1 - \xi_0) \right], \tag{1}$$

where C_d is the damage rate coefficient, power index n and function $D(\alpha)$ control the shape and size of the yield surface. The solution of the 1-D equilibrium equation ($\partial\sigma/\partial x = 0$) gives uniform stress even for a heterogeneous material with damage-dependent Young's modulus:

$$E(x, t) = E_0 [1 - \alpha(x, t)], \tag{2}$$

where E_0 is the Young's modulus of the intact material. The linear relation between Young's modulus and the damage is common for many damage rheology models, and it is analogous to the complete 3-D model formulations. We study damage evolution in a sample with a unit length and fixed displacements at the boundaries, $u(0, t) = 0$, and $u(1, t) = u_0$. Integrating the stress–strain relation ($\sigma = E(x, t) \cdot \varepsilon(x, t)$) over the unit length of the sample, using the displacement boundary conditions, and eq. (2) gives the time-dependent stress

$$\sigma(t) = \frac{\varepsilon_0(t)}{\Omega}, \tag{3}$$

where $\Omega = \int_0^1 \frac{dx}{(1-\alpha)}$, and ϵ_0 is the elastic strain applied to the sample, which is equal to u_0 divided by the sample length. The strain distribution is given by

$$\varepsilon(x, t) = \frac{\varepsilon_0(t)}{\Omega \cdot (1 - \alpha(x, t))}. \tag{4}$$

Substituting (4) into (1) leads to the equation of the damage evolution for the investigated sample:

$$\frac{d\alpha}{dt} = C_d \varepsilon_0^2 [(1 - \alpha)\Omega]^{-2} \times \left[D(\alpha)(-\varepsilon_0)^n ((1 - \alpha)\Omega)^{-n} - (1 + \xi_0) \right]. \tag{5}$$

The evolution equation for the damage accumulation is only defined for conditions where the expression in the right square brackets is positive. For a non-uniform damage distribution, it grows only in the points where the strain values are above the yield surface. For constant D-values, the yield surface remains unchanged, and damage keeps growing and strongly localizing until failure (Lyakhovsky *et al.* 1997). Distributed strain and smoothing of the damage distribution are possible for decreasing D-values, which promote an increase in the size of the yield surface. Fast-growing yield surface relative to evolving load conditions may bring the yield path back to the stable conditions and thus smoothing the damage distribution. To realize such scenario, a strong damage dependency of the D-values should be adopted. Considering this condition, we suggest an exponential $D(\alpha)$ dependency:

$$D(\alpha) = D_1 \exp(D_2 \alpha), \tag{6}$$

where positive coefficient D_1 stands for the initial D-value of the damage-free material, and negative D_2 controls its decrease with the growing damage.

Substituting (6) into the damage growth eq. (5) allows to define a critical strain

$$\varepsilon_{cr} = -\left(\frac{1 + \xi_0}{D_1} \right)^{\frac{1}{n}}, \tag{7}$$

corresponding to the onset of damage accumulation in the intact material ($\alpha = 0$). After scaling the overall strain and stress to the critical values, $\varepsilon_*(t) = \varepsilon_0/\varepsilon_{cr}$, $\sigma_*(t) = \sigma/E_0\varepsilon_{cr}$, and using (6), the damage kinetic eq. (5) is re-arranged to a slightly simplified form

$$\frac{d\alpha}{dt} = \chi \varepsilon_*^2 (1 - \alpha)^{-2} \Omega^{-2} \left[\exp(D_2 \alpha) \varepsilon_*^n ((1 - \alpha)\Omega)^{-n} - 1 \right], \tag{8}$$

where $\chi = C_d \varepsilon_{cr}^2 (1 + \xi_0)$. This form of the damage growth equation shows that the obtained damage pattern and distributed or localized strain depend only on two parameters, that is, applied deformation ε_* and the coefficient D_2 controlling the coupling between damage and the size of the yield surface. D_1 is included in the kinematic coefficient χ and does not affect the spatial damage evolution.

2.3 Modelling of the Kaiser effect

In this section, we present an analytical estimation of the FR change under constant strain rate. We assume that under low confining pressures damage accumulation process consists mostly of fracture processes resulting from intergranular cracking, breaking of cemented grain boundaries, grain boundary sliding and grain rotation boundaries. We assume that the damage parameter α correlates with the cumulative AE counts (Hamiel *et al.* 2004a; Choens & Chester 2014), and that the onset of damage can be determined by the onset of AE, thus allowing us to infer the quality of the Kaiser effect and FR trend.

We start with a simplified case of a homogeneous and initially damage-free sample ($\alpha(0) = 0$) loaded at a constant strain rate $\dot{\varepsilon}_*$. Once loading reaches the yield criterion, damage starts to accumulate and the yield criterion changes. After a small amount of damage is accumulated, the sample is unloaded and then reloaded at the same strain rate as the previous cycle, until yielding is achieved again. This new yield condition is reflected by the FR of the Kaiser effect. In the case of a homogeneous damage distribution, $\alpha = \alpha(t)$, the Ω value in eq. (4) becomes equal to $\Omega(t) = 1/(1-\alpha(t))$, and the strain distribution within the sample is also homogeneous, $\varepsilon_*(x,t) = \varepsilon_*(t)$. Substituting the above Ω value in eq. (8) gives the onset of AE at the strain value equal to $\varepsilon = \exp(-(D_2/n)\alpha)$, and using the corresponding stress, the model FR is defined as

$$\mathrm{FR} = \frac{\sigma_{*\mathrm{AE}}}{\sigma_{*\mathrm{Max}}} = \frac{(1-\alpha)\exp\left(-\frac{D_2}{n}\alpha\right)}{\sigma_{*\mathrm{Max}}}, \tag{9}$$

where $\sigma_{*\mathrm{Max}}$ is the peak stress obtained during the first of two consecutive cycles. During a loading cycle the stress continues to grow with increasing strain. In some cases, it reaches the ultimate value, $\sigma_{*\mathrm{ultimate}}$, and then slightly decreases before the unloading due to a strong decrease in the effective Young's modules. In most cases, such a decrease leads to a stress drop and macroscopic failure of the sample. In our calculations, we distinguish between these cases and use two different definitions for the maximum stress value:

$$\sigma_{*\mathrm{Max}} \cong \begin{cases} (1-\alpha)\,\varepsilon_* \text{ for Max}\,(\sigma_*) < \sigma_{*\mathrm{ultimate}} \\ \sigma_{*\mathrm{ultimate}} \text{ for Max}\,(\sigma_*) = \sigma_{*\mathrm{ultimate}} \end{cases}. \tag{10}$$

The model with constant yield surface ($D_2 = 0$) predicts that the FR decreases proportionally to the strain ($\mathrm{FR} = 1/\varepsilon_*$), until ultimate stress is reached. For a constant strain rate, $\varepsilon_* \propto \dot{\varepsilon}_* t$, the FR decreases at the initial stage of loading with the slope equal to the strain rate. The analytical solution presented below demonstrates that this tendency of the FR decrease is general for all negative D_2 values. An analytical solution is obtained for the homogeneous damage distribution for which the growth eq. (8) is reduced to

$$\frac{\mathrm{d}\alpha}{\mathrm{d}t} = \chi\varepsilon_*^2\left[\exp(D_2\alpha)\,\varepsilon_*^n - 1\right]. \tag{11}$$

We consider slow constant loading rates ($\dot{\varepsilon}_* = \mathrm{const}$), such that the damage closely follows the equilibrium damage value $\alpha_0(t) = -(n/D_2)\ln(\varepsilon_*(t))$. We find the solution of the eq. (11) in the form of small damage deviation ($\delta\alpha \ll 1$) from this equilibrium solution:

$$\alpha(t) = \alpha_0(t) - \delta\alpha(t) = -\frac{n}{D_2}\ln(\varepsilon_*(t)) - \delta\alpha(t). \tag{12}$$

Keeping first-order terms for small $\delta\alpha$ leads to

$$\frac{\mathrm{d}}{\mathrm{d}t}(\delta\alpha) = \delta\alpha(t)\,D_2\chi\varepsilon_*^2(t) + \frac{\mathrm{d}}{\mathrm{d}t}(\alpha_0(t)), \tag{13}$$

which has the solution

$$\delta\alpha(t) = \mathrm{e}^{f(t)}\int_0^t \frac{\mathrm{d}\alpha_0(t)}{\mathrm{d}t}\mathrm{e}^{-f(t)}\mathrm{d}t, \tag{14}$$

where $\dot{f}(t) = D_2\chi\varepsilon_*^2(t)$. Integrating (14), substituting into (12) and then into (9) leads to a semi-analytical approximation of the FR. At a very initial stage of loading, ($\mathrm{e}^{f(t)} = \mathrm{e}^{-f(t)} \approx 1$), $\delta\alpha$ can be approximated as $\delta\alpha(t) \sim (\mathrm{d}\alpha_0(t)/\mathrm{d}t)t$. Finally, substituting this value into (9) and using (10) gives the approximation for the initial stage of loading for negative D_2 values

$$\mathrm{FR} = 1 - \dot{\varepsilon}_* t. \tag{15}$$

3 RESULTS

3.1 The Kaiser effect

The results of the analytical and numerical solutions are shown in Fig. 4 for two different strain rate values and different D_2 values. Green lines represent the linear FR decrease at very initial stages using the approximation (15). This expression determines that for a constant strain rate experiment, the FR will always initially decrease with a slope equal to $\dot{\varepsilon}_*$. The red lines in Fig. 4 represent the semi-analytical solution by the integration of (14). Since $\alpha_0(t)$ increases logarithmically in time and rate of its change decreases, the solution of (14) predicts that $\delta\alpha \to 0$ at a certain stage of growth, giving minimum $\delta\alpha$ at a certain stage. At this point, depending on whether $\sigma_{*\mathrm{ultimate}}$ was reached, the FR either starts increasing towards $\mathrm{FR} \to 1$ ($\sigma_{*\mathrm{Max}} < \sigma_{*\mathrm{ultimate}}$), or reaches an inflection point and continues decreasing ($\sigma_{*\mathrm{Max}} = \sigma_{*\mathrm{ultimate}}$). FR increase is clearly recognized in the case with $D_2 = -3$ shown in Fig. 4(b) and less explicit at a lower strain rate shown in Fig. 4(a). FR value linearly decreases with time at the very initial stage of loading, then slightly increases and finally decreases towards failure. For larger $D_2 = -2$ value (also shown in Fig. 4) the inflection point is clearly recognized. When the ultimate strength is reached so that $\sigma_{\mathrm{Max}} = \sigma_{\mathrm{ultimate}}$, FR becomes linearly dependent on $\sigma_{*\mathrm{AE}} = (1-\alpha)\,\varepsilon_*(t)$, and decreases towards zero as $\alpha \to 1$.

The numerical code was developed for an explicit solution of the damage growth eq. (8) and for calculating the FR for any given initial damage distribution. Numerical simulations and analytical solutions were done for many cases, in which the time until unloading was changed, and the new yield and damage was calculated. Reloading the sample back to yield allowed the calculation of the FR for each unloading time. Numerical results for the damage-free initial conditions (blue stars in Fig. 4) match the analytical solution, including the initial decrease followed by a certain increase or an inflection point in the FR.

In most studies dealing with the Kaiser effect, the experimentally estimated FR is presented versus stress, as shown in Fig. 2. Moreover, in most rock mechanics experiments, loading could be increased up to the ultimate stress. A negative slope of the stress–strain curve leads to instability, and fast macroscopic failure occurs if the loading system is not equipped by a sensitive servo-control system (e.g. Lockner *et al.* 1992). Since the stress–strain curve of the rock sample accumulating AE (damage) is nonlinear, it is not possible to make a direct comparison between simulated FR of Fig. 4 with experimental data. Therefore, Fig. 5 shows FR versus stress, compatible with data reported by Li & Nordlund (1993), to the ultimate stress marked with stars at the end of each curve. FR is measured from the onset of the damage accumulation at 20 MPa in this model. Similar to Fig. 4, all the curves linearly decrease with the onset of damage, but soon after start to deviate according to the model parameters. The most pronounce FR decrease (black line in Fig. 5) corresponds to the model with $n = 2$ and $D_2 = -4$, as is expected for larger negative D_2 values. Even for a very low damage

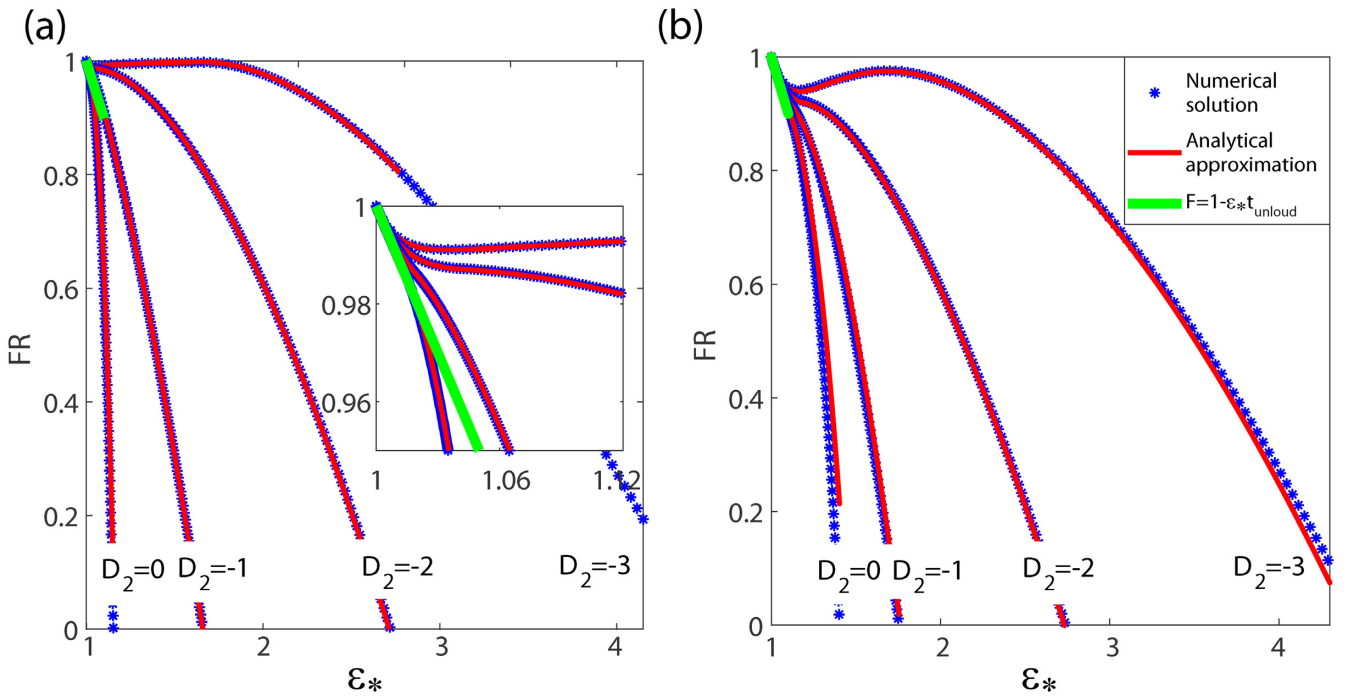

Figure 4. The FR of two consecutive loading cycles as a function of the normalized unloading strain of the first cycle. The results are for a homogeneous, initially intact sample ($\alpha(0) = 0$). The simulated sample was loaded at a constant strain rate, immediately unloaded at ε_* and then reloaded at the same rate until $\alpha = 1$. Blue stars show the current numerical results—each star represent a single simulation. The red line shows the results of the analytical approximation (see the text). The green line shows the initial linear dependency of the FR on the strain rate. Panel (b) shows the results for a strain rate 10 times larger than that given in panel (a).

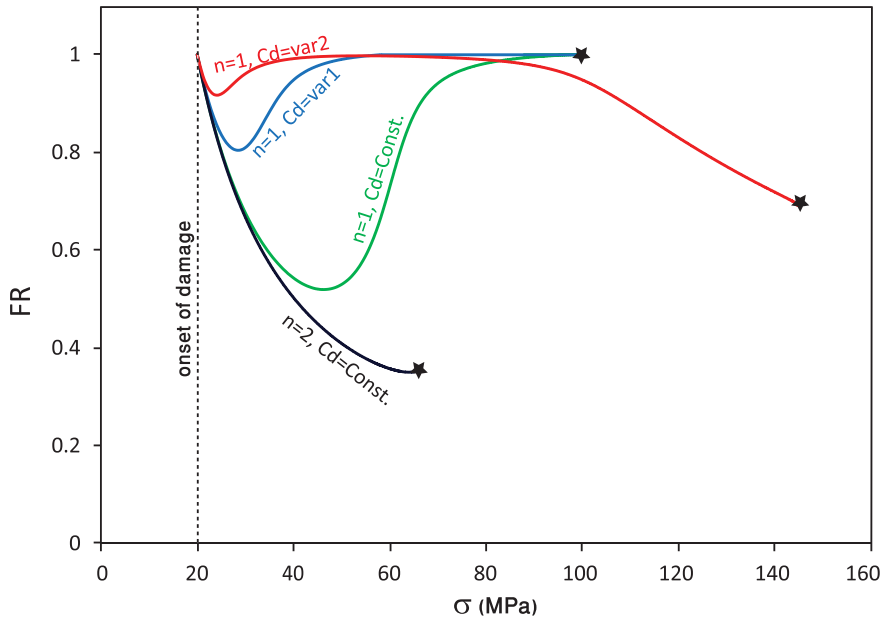

Figure 5. FR versus stress for different model realizations with power index $n = 1,2$; $D_2 = -4$; constant and stress-dependent damage rate coefficient.

accumulation rate (damage rate is three orders of magnitudes below the strain rate), the ultimate stress is well below the strength of the rock samples of Fig. 2 (70 MPa versus 130 MPa). A larger ultimate stress value is predicted by a model with lower value of the power index $n = 1$. With the reduced ratio between damage rate to the strain rate to 0.1, the ultimate stress reaches about 100 MPa (green line in Fig. 5), and FR decrease is less pronounced. In these two cases, the damage rate coefficient is constant, and the shape of both green and dark blue curves is far from the general tendency of the FR data of Fig. 2.

Comparing measured and predicted strength of granite samples under various loading rates and confining pressures, Lyakhovsky *et al.* (2005) suggested that experimental observations are fitted well with constant damage rate coefficient, C_d, under high confining

pressure. At low confining pressures, the damage rheology model with constant C_d values significantly underestimated the rate of damage accumulation and overestimated the rock strength. Therefore they suggested exponentially stress-dependent C_d, which strongly decreases with increasing load:

$$C_d(\sigma) = C_{d0} + C_{d1}\ \exp(\sigma/\sigma_0). \tag{16}$$

For Westerly granite, a stress-dependent C_d decreases with a characteristic scale of $\sigma_0 = 50$ MPa (Lyakhovsky *et al.* 2005). A similar exponential decrease in C_d used by Panteleev *et al.* (2020), who analysed damage accumulation in Darley Dale sandstone under 4 MPa confining pressure. With this stress dependent C_d, the decrease of FR (blue line in Fig. 5) is much smaller, with no change of the strength (compare with green line). This model was run with $C_{d0} = C_{d1}$ equal to the strain rate and $\sigma_0 = 40$ MPa. A significant increase of C_{d1} by two orders of magnitudes further reduces FR decrease during the initial stage of loading (red line in Fig. 5), and a similar decrease of C_{d0} by two orders of magnitudes leads to gradual FR decrease at large stresses. The shape of the red line Fig. 5 is close to the FR change of the Bjorka marble data of Fig. 2.

The simulated FR curves of Fig. 2 are achieved with an additional tuning of the model parameters. The curves reasonably reproduce the general FR tendency for Bjorka marble, Malmberget and Bolmen gneiss. For all cases, the power index n is 1, $D_2 = -3.8$ for Bjorka marble and Malmberget gneiss, and $D_2 = -4.5$ used for Bolmen gneiss. The characteristic stress value $\sigma_0 = 45,\ 16,$ and 22 MPa, and the ratio C_{d1}/C_{d0} is 10^6, 10^3, and 10^5 for Bjorka marble, Malmberget and Bolmen gneiss, respectively. We note here a non-uniqueness of the model parameters with the lack of detailed information on the experimental settings and additional experiments results under different confined conditions. The presented model results in Figs 2 and 5 demonstrate the general ability of the model in reproducing the Kaiser effect and tendency in the FR change.

3.2 Distributed versus localized damage accumulation

We utilize the same numerical code to study the evolving spatial distribution of the damage and strain in the sample. To distinguish between effects associated with the rate of damage growth and the rate of loading, we apply an instantaneous load and then fixed displacements at the edges of the sample. The rate of the strain and damage change in the sample is controlled by a single model parameter $\chi \propto C_d/D_1$ (damage kinetic coefficient). Therefore, all the results are shown versus non-dimensional time, $t_* = t \cdot (C_d/D_1)$. In this case, the results depend on the applied strain (ε_*), damage-dependent change on the yield surface (D_2), and the initial damage distribution ($\alpha_0(x)$). In the case of the constant yield surface ($D_2 = 0$) singular damage and strain localization is obtained (not shown here), similarly to the local damage rheology models (e.g. Lyakhovsky *et al.* 1997). However, an evolving yield with $D_2 < 0$ may lead to a stabilization of the damage growth and prevent strain localization. We demonstrate this behaviour for $D_2 = -3$ using a simplified initial box-like damage distribution with a small area of 10% of the sample length with initial damage level $\alpha_2 = 0.3$, which differs from the rest of the sample with a damage level $\alpha_1 = 0.2$. The box-like spatial damage distribution is preserved during evolution (Figs 6a and b), while the difference between the evolving damage values, $\Delta\alpha(t) = \alpha_2(t) - \alpha_1(t)$, determines the tendency of the system to exhibit localized ($\mathrm{d}\Delta\alpha/\mathrm{d}t > 0$) or distributed ($\mathrm{d}\Delta\alpha/\mathrm{d}t < 0$) damage distribution. Under relatively high strain, ($\varepsilon_* = 2$), the sample undergoes damage localization; damage within the initially weak area increases much faster than its surroundings (Fig. 6a) and $\Delta\alpha$ steeply increases with time towards total failure (Fig. 6c). Under lower strain ($\varepsilon_* = 1.4$), only very minor damage growth is predicted in the initially weak zone, while most of the growth occurs in the surrounding material (Fig. 6b). The difference between damage values, $\Delta\alpha$, decreases towards a constant value (Fig. 6d). These results mean that under different loading conditions the same material can undergo strain and damage localization and macroscopic failure or distributed damage accumulation with a steady-state condition.

Fig. 7 shows the result of a parametric search study for different loading conditions, yielding parameters, and initial damage distribution. Two different cases are considered. In one case, $\alpha_2 \geq \alpha_1$ representing a small embedded weak zone as in Fig. 6. Simulations with this initial condition form the upper triangle part of each diagram. The lower triangle corresponds to the strong embedded damage zone with $\alpha_2 < \alpha_1$. The coloured fields of each diagram correspond to different trends of damage evolution. Yellow fields correspond to the stable condition below the yield surface. The stable area occupies almost the whole diagram (c) corresponding to a relatively high $D_2 = -4$ and small loading $\varepsilon_* = 1.2$ since large negative D_2 values are a stabilizing factor, and low strains lead to less pronounced damage. Making D_2 values less negative along with load increase leads to shrinking the stable zone, increasing the blue area where localized damage is predicted. In diagram (g), the blue zone occupies significant part of the whole area. Arrows inside this zone show the general tendency of the damage evolution. Once localization conditions for weak inclusion (upper triangle of the diagrams) are realized, damage evolves towards failure, while for the strong inclusion (lower triangle), the background (α_1) damage value increases until the stable state is reached. Red zones appear in some diagrams pointing to the conditions of the distributed damage eliminating spatial damage variations. In this regime, damage evolves towards a stable state. With the same model parameters (i.e. D_2 value) the geometry of these zones is very sensitive to the applied load. The model with $D_2 = -3$ and the same initial damage distribution predicts distributed damage at the intermediate strain level [green star in diagram (e)] and localized damage at the elevated strain [red star in diagram (h)]. The damage evolution for these cases is shown in the previous Fig. 6.

An additional series of simulations with initial random damage distribution $\alpha(0) = 0.2 \pm 0.02$, strain, $\varepsilon_* = 1.8$ and different D_2 values (Fig. 8) shows the effect the small change in the D_2 values from -3.0 to -3.25 on the mode of the damage evolution. For $D_2 = -3.0$ (Fig. 8a), the damage growth significantly accelerates in the zones with elevated initial damage values, finally forming a spike around $x \sim 0.3$. Similar to Figs 6(c) and (d), we use $\Delta\alpha = \alpha_{\mathrm{Max}} - \alpha_{\mathrm{Min}}$ as a measure of the spatial damage heterogeneity. $\Delta\alpha$ slowly increases during most of the loading period (Fig. 8b), but steeply increases in an explosive manner just prior to failure. The opposite behaviour is predicted by the model with slightly more negative $D_2 = -3.25$ (Figs 8c and d). The same initial damage grows with an almost similar rate in the whole sample and is stabilized at values $\alpha < 0.4$ (Fig. 8c). The spatial damage variability (Fig. 8d) slightly increases at the initial stage of evolution, but then gradually decreases ($\Delta\alpha \to 0$). These results obtained with the same initial and loading conditions, show the transition between different modes of damage accumulation due to small variations in the single model parameter D_2 controlling the coupling damage-dependent yield surface change.

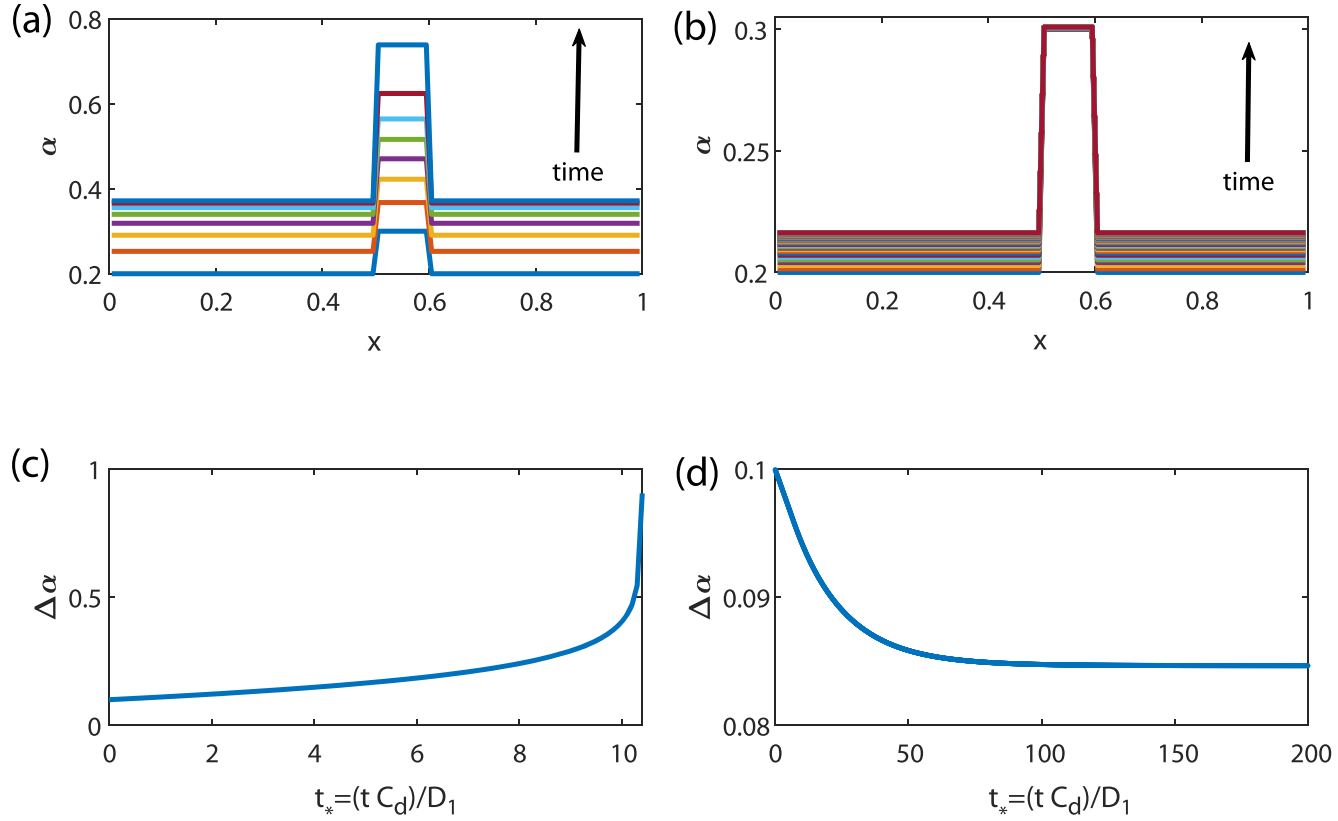

Figure 6. Time evolution of the spatial damage distribution (a and b) and the damage contrast $\Delta\alpha$ (c and d) in a sample with a bimodal damage distribution. The initial damage value of 90% of the sample is $\alpha_1 = 0.2$, the remaining 10% of the sample is assigned with the initial value of $\alpha_2 = 0.3$. The area with α_2 damage value can be viewed as a damaged zone. The simulations are conducted with the same $D_2 = -3$ and two different strain values: $\varepsilon_* = 2$ (a and c) and $\varepsilon_* = 1.4$ (b and d).

3.3 The Kaiser effect and damage localization

We study the connection between the modes of damage evolution, distributed versus localized, and the Kaiser effect quality expressed by FR. The results shown in Fig. 9 are obtained using the same numerical procedure with random initial damage distribution $\alpha(0) = 0.2 \pm 0.02$, but applying a constant strain rate. As in previous simulations (Fig. 4), the FR is calculated using two consecutive loading cycles and is presented as a function of the normalized unloading time (blue line in Fig. 9). Due to relatively high $D_2 = -3.45$ and low strain at the initial stage of loading, FR remains high during a relatively long stage until about $\varepsilon_* \sim 1.7$. At the following stage, the decreases of the FR value slowly accelerates and drops below FR $= 0.9$ at the final stage towards failure. The red line on the same plot shows the measure of the spatial damage heterogeneity, $\Delta\alpha = \alpha_{\mathrm{Max}} - \alpha_{\mathrm{Min}}$. Similarly to the previous results (Figs 6 and 8), this difference points to transition from a distributed damage accumulation mode with decreasing spatial damage variability to the localization mode. The clear minimum (star on the red line) shows that this transition occurs around $\varepsilon_* \sim 1.7$, close to the onset of the FR decrease. The comparison between blue and red lines shown on the same plot in Fig. 9 suggests that high FR values are expected during the loading stage with a distributed mode of the damage accumulation. This and other simulation results under different conditions (not shown here) support that for highly damage dependent yield surfaces, high FR values are expected during the loading stage corresponding to the distributed damage accumulation mode. The damage and strain localization occurs under conditions corresponding to a steep FR decrease.

4 DISCUSSION

The presented results highlight the coupling between the damage and the yield surface growth and show its effect on damage localization patterns, as well as the quality of the Kaiser effect as reflected by the FR. Weak coupling between the damage and yield surface growth results in an immediate decrease of the FR. A strongly coupled damage—yield surface growth result with an initial decrease of the FR and then an increase to a value close to 1 until approaching the samples' ultimate strength. When the sample approaches failure FR $\rightarrow$ 0. The change in the FR has been commonly noted in laboratory experiments yet is rarely quantified (Zhang *et al.* 2018). Li & Nordlund (1993) presented results demonstrating FR values for three different types of rocks (Fig. 2). Coloured lines in Fig. 2 show simulations of FR various stress. Reasonable agreement between the general tendency of the experimentally observed change of the FR values with loading and modelling results provides validating the developed model. Comparing the model results obtained with constant and stress-dependent damage rate coefficient (Fig. 5) emphasizes its significant increase under low-stress values.

Localization patterns are connected to the coupling between yield surface and damage, represented here by D_2. Crystalline rocks that show strong localization patterns are expected to have D_2 values close to zero. A weak coupling between damage and yield surface does not allow strain hardening; thus damage continues to accumulate in the most damaged areas, promoting unstable localized fracturing. Rocks with damage-dependent yield surface controlled by negative D_2 values exhibit a significant distributed damage stage.

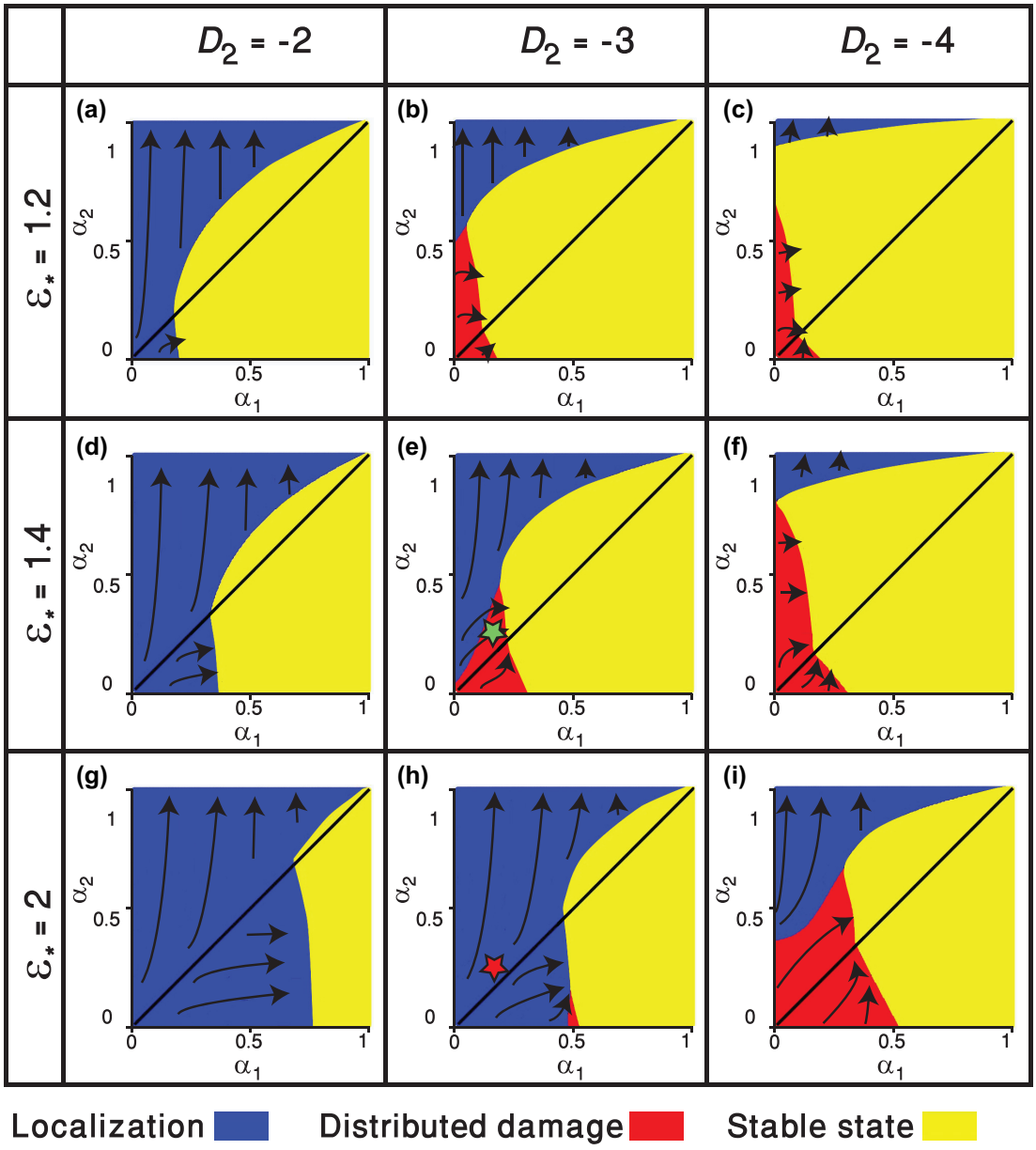

Figure 7. A set of diagrams demonstrating different modes of damage evolution. The yellow areas mean stable damage distribution, the blue areas mean damage localization and the red areas mean distributed damage eliminating spatial damage variations. Each diagram represents simulations with bimodal initial damage distribution with α_1 and α_2 values, similar to Fig. 6. The simulations of Fig. 6 are marked by red and green stares. Different panels correspond to different applied constant strain, ε_*, and yield cap growth parameter, D_2, values.

Every column in Fig. 6 can be viewed as snapshots of a continuous laboratory experiment with increasing loading. Similar to laboratory experiments, the model predicts that initial loading starts with stable conditions (yellow), and with increasing loading, the sample gets into the mode of distributed damage (red) and with further loading becomes localized (blue). For example, the green and red stars in Figs 6(e) and (h) represent the transition from a distributed to a localized mode of damage. Two types of modelling: cyclic loading for Kaiser effect and continuous loading for localization, shown in Fig. 9, demonstrate that the transition between distributed and localized modes of damage is correlated with the onset of a steep decrease in FR.

Some works have experimentally examined the overall yield surface evolution of porous rocks (Bedford *et al.* 2018, 2019), but the connection between the rocks' physical properties and the shape of the yield surface is not clear. The presented model allows a constraint of the yield surface parameters by monitoring AE during cyclic load and estimating FR. The ratio D_2/n can be estimated by rearranging (9):

$$\frac{D_2}{n} = -\frac{E_0}{E_0 - E_{\text{eff}}} \ln\left(\frac{\text{FR}\,\sigma_{\text{Max}}}{E_{\text{eff}}\varepsilon_{\text{cr}}}\right) \tag{17}$$

Using this relation the D_2/n ratio can be estimated from the FR value and the effective Young's modulus from measured stress–strain curves. D_1 and n can be independently constrained by determining the shape of the yield surface for an intact rock by a series of loading experiments under different confining pressures.

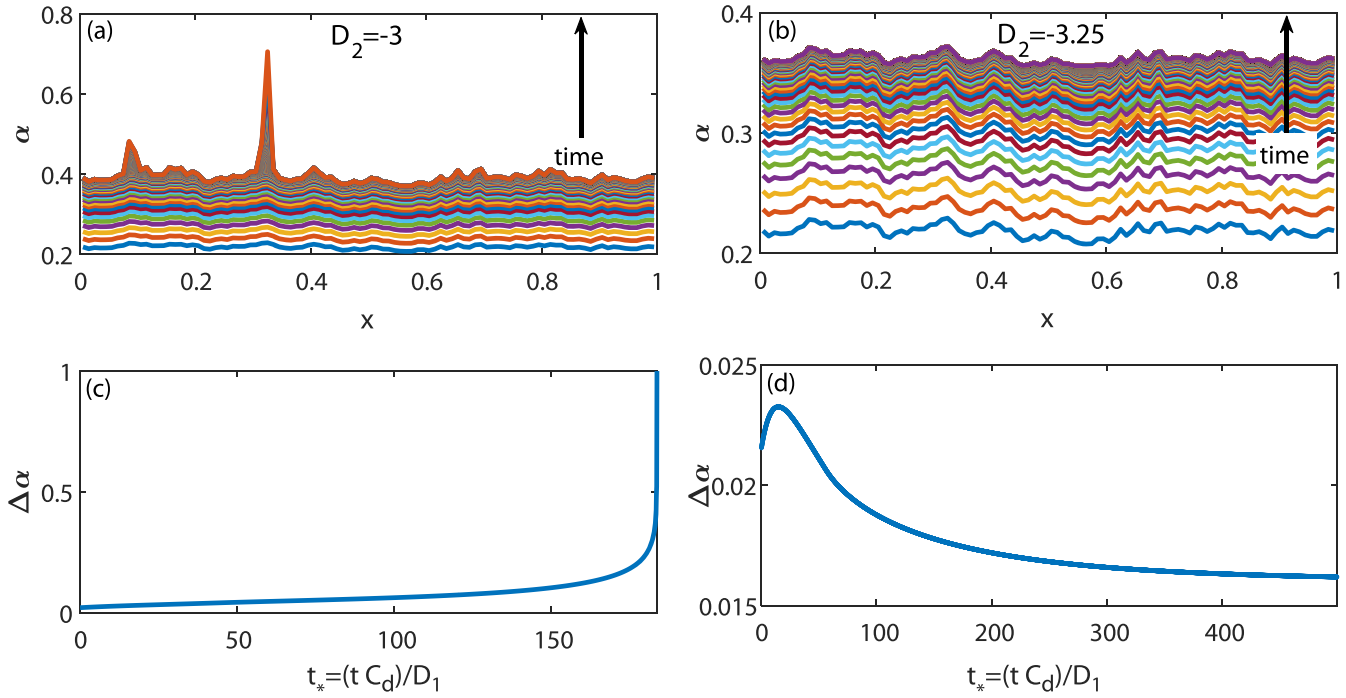

Figure 8. Time evolution of the spatial damage distribution (a and b) and the damage contrast $\Delta\alpha$ (c and d) in a sample with initial random damage distribution $\alpha(0) = 0.2 \pm 0.02$, constant applied strain $\varepsilon_* = 1.8$ and a slightly different yield cap growth parameter $D_2 = -3.0$ (a and b) and $D_2 = -3.25$ (c and d). The simulation shows that the transition from localized failure (a and b) to the distributed damage occurs at small variations of the D_2 value. The difference between the maximum and minimum damage, $\Delta\alpha = \alpha_{\mathrm{Max}} - \alpha_{\mathrm{Min}}$, steeply increases towards failure (b), while for more negative D_2 (d) after some small increase at the initial stage, $\Delta\alpha$ gradually decreases.

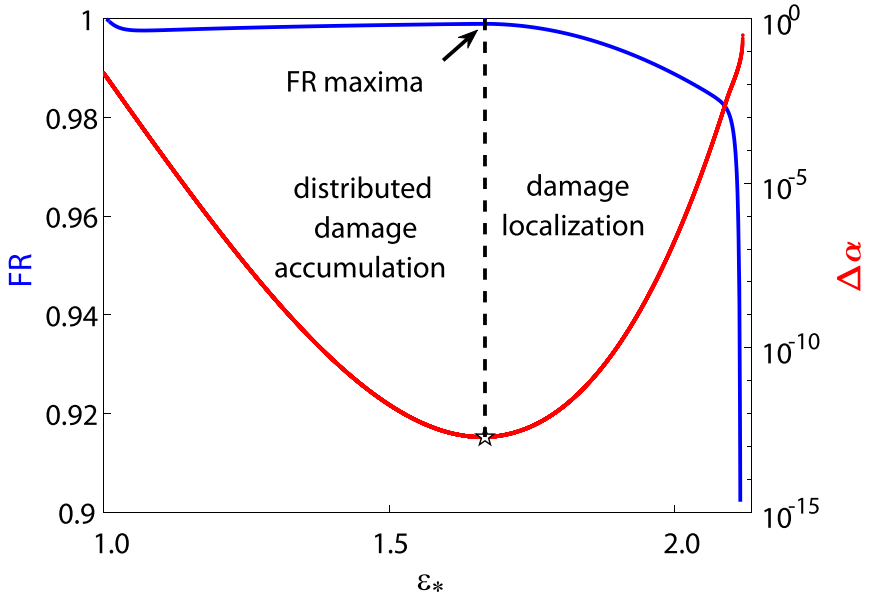

Figure 9. Simulated FR (the blue line) and the measure of the spatial damage heterogeneity ($\Delta\alpha = \alpha_{\mathrm{Max}} - \alpha_{\mathrm{Min}}$— red line) for a model with initial random damage distribution $\alpha_0 = 0.2 \pm 0.02$, yield cap growth parameter $D_2 = -3.45$ and constant strain rate. The white star and the dashed black line mark the FR local maxima that coincides with the transition of the system from the distributed mode of the damage accumulation to localization.

Although mostly observed under controlled conditions in the lab experiments, the Kaiser effect has been observed in different scales and settings. It was tested for practical use as a possible indicator for meters long concrete beam failure (Sagar *et al.* 2015) and was possibly observed during AE monitoring of bridges (Nair & Cai 2010). The effect was also observed in several locations on a kilometre-scale geological setting, as seismicity induced by pressure change due to volcanic activity (Heimisson *et al.* 2015), and groundwater level changes (Simpson & Negmatullaev 1981). Fault localization processes have been observed on different scales (Ben-Zion & Sammis 2003), including tectonic settings (e.g. Marco 2007). However, there is an ongoing discussion regarding the similarity of these process on different scales (Ben-Zion & Sammis 2003). Our formulation is dimensionless, suggesting that

the connection between the FR and localization process may be observed at all scales from micro fractures to plate-boundary faulting, thus, in cases where highly negative D_2 values are matched to a problem, changes in the FR trend may help to predict damage localization process and failure.

5 CONCLUSIONS

We study the effect of damage dependent yield surface on localized/distributed damage accumulation and the Kaiser effect using analytical and numerical methods. Under sufficient strain, a constant or weakly coupled damage—yield surface growth results in strong and fast damage-localization and failure—as seen in crystalline rocks. A strong coupling between damage and yield surface growth promotes, under certain conditions, distributed damage accumulation, and for adequate strain paths, induces transition between phases of localized and distributed damage accumulation. This type of dependency also allows the material to regain stability after initial damage increase and can promote the consecutive formation of deformation bands prior to faulting.

The quality of the Kaiser effect produced by rock samples consecutive loading cycles is determined by the FR. While for weak damage—yield growth coupling the FR deteriorates between consecutive cycles, for a strong coupling, the FR remains close to one and starts dropping upon approaching ultimate strength and deteriorates towards zero as the sample reaches failure. For strong damage—yield surface coupling, the FR decrease correlates with the transition between distributed and localized damage accumulation. We suggest that a better understanding of FR trends can be used to determine the yield surface dependency on damage and helps predict different damage localization patterns.

ACKNOWLEDGEMENTS

The paper was benefitted from constructive comments by Jess McBeck, anonymous reviewer and the Editor Alexis Maineult. The study was supported by grant from the United States-Israel Binational Science Foundation (BSF 2014036). WZ acknowledges the partial support from NSF EAR-1761912. SM acknowledges support of the Israel Sinence Foundation 1645/19

REFERENCES

Antonellini, A.M., Aydin, A. & Pollard, D., 1994. Microstructure of deformation bands in porous sandstones at Arches National Park, Utah, *J. Struct. Geol.,* **16**(7), 941–959.

Aydin, A. & Johnson, A.M., 1983. Analysis of faulting in porous sandstones, *J. Struct. Geol.,* **5**(1), 19–31.

Baud, P., Klein, E. & Wong, T., 2004. Compaction localizetion in porous sandstones: spatial evolution of damage and acoustic emission activity, *J. Struct. Geo.,* **26**:603–624.

Baud, P., Vajdova, V. & Wong, T., 2006. Shear-enhanced compaction and strain localization: Inelastic deformation and constitutive modeling of four porous sandstones, *J. geophys. Res.,* **111**(B12), doi:10.1029/2005JB004101.

Bedford, J.D., Faulkner, D.R, Leclère, H. & Wheeler, J., 2018. High-resolution mapping of yield curve shape and evolution for porous rock: the effect of inelastic compaction on porous bassanite, *J. geophys. Res.,* **123**(2), 1217–1234.

Bedford, J.D., Faulkner, D.R., Wheeler, J. & Leclère, H., 2019. High-resolution mapping of yield curve shape and evolution for high porosity sandstone, *J. geophys. Res.,* **124**(6), 5450–5468.

Ben-Zion, Y. & Sammis, C.G., 2003. Characterization of fault zones, *Pure appl. Geophys.,* **160**(3-4), 677–715.

Berdichevsky, V.L., 2009. *Variational Principles of Continuum Mechanics,* Springer-Verlag.

Bernard, X. Du., Labaume, P., Darcel, C., Davy, P. & Bour, O., 2002. Cataclastic slip band distribution in normal fault damage zones, Nubian sandstones, Suez rift, *J. geophys. Res.,* **107**(B7), doi:10.1029/2001JB000493.

Biot, M.A., 1955. Theory of elasticity and consolidation for a porous anisotropic solid, *J. Appl. Phys.,* **26**(2), 182–185.

Carroll, M.M., 1991. A critical state plasticity theory for porous reservoir rock, *in Recent Advances in Mechanics of Structured Continua,* **Vol. 117,** pp. 1–8, eds Massoudi M., Rajagopal K.R., American Society of Mechanical Engineers.

Choens, R.C. & Chester, F.M., 2014. Characterizing damage evolution and yield surfaces for berea sandstone under triaxial loading as a function of effective pressure, in *48th US Rock Mechanics/Geomechanics Symposium,* American Rock Mechanics Association.

Das, A., Tengattini, A., Nguyen, G.D., Viggiani, G., Hall, S.A. & Einav, I., 2014. A thermomechanical constitutive model for cemented granular materials with quantifiable internal variables. Part II–validation and localization analysis, *J. Mech. Phys. Solids,* **70,** 382–405.

de Groot, S.R. & Mazur, P., 1962. *Nonequilibrium Thermodynamics,* pp. 510, North-Holland Publishing Co.

DiMaggio, F.L. & Sandler, I.S., 1971. Material model for granular soils, *J. Eng. Mech.,* **97**(EM3), 935–950.

Fitts, D.D., 1962. *Nonequilibrium Thermodynamics,* 173 pp., McGraw-Hill Book Company.

Fossen, H., Schultz, R.A., Shipton, Z.K. & Mair, K., 2007. Deformation bands in sandstone: a review, *J. geol. Soc. Lond.,* **164**(4), 755–769.

Gajst, H., Weinberger, R., Zhu, W., Lyakhovsky, V., Marco, S. & Shalev, E., 2018. Effects of pre-existing faults on compaction localization in porous sandstones, *Tectonophysics,* **747,** 1–15.

Goodman, R.E., 1963. Sub audible noise during compression of rocks. *Bull. geol. Soc. Am.,* **74**(4), 487–490.

Grueschow, E. & Rudnicki, J.W., 2005. Elliptic yield cap constitutive modeling for high porosity sandstone. *Int. J. Solids Struct.,* **42**(16–17), 4574–4587.

Hamiel, Y., Liu, Y., Lyakhovsky, V., Ben-Zion, Y. & Lockner, D., 2004a. A viscoelastic damage model with applications to stable and unstable fracturing, *Geophys. J. Int.,* **159**(2004), 1155–1165.

Hamiel, Y., Lyakhovsky, V. & Agnon, A., 2004b. Coupled evolution of damage and porosity in poroelastic media: theory and applications to deformation of porous rocks, *Geophys. J. Int.,* **156**(3), 701–713.

Heimisson, E.R., Einarsson, P., Sigmundsson, F. & Brandsdóttir, B., 2015. Kilometer-scale Kaiser effect identified in Krafla volcano, Iceland, *Geophys. Res.,* **42**(19), 7958–7965.

Holcomb, D.J., 1993a. Observations of the Kaiser effect under multiaxial stress states: implications for its use in determining in situ stress, *Geophys. Res.,* **20**(19), 2119–2122.

Holcomb, D.J., 1993b. General theory of the Kaiser effect, *Int. J. Rock Mech. Min. Sci. Geomech. Abstr.,* **30**(7), 929–935.

Issen, K.A. & Rudnicki, J.W., 2000, Conditions for compaction bands in porous rock, *J. geophys. Res.,* **105**(B9), 21 529–21 536.

Jaeger, J.C., Cook, N.G.W. & Zimmerman, R., 2007. *Fundamentals of Rock Mechanics,* John Wiley & Sons.

Kaiser, J., 1953. Erkenntnisse und Folgerungen aus der Messung von Geräuschen bei Zugbeanspruchung von metallischen Werkstoffen, *Arch. Eisenhuettenwes.,* **24**(1-2), 43–45.

Kurita, K. & Fujii, N., 1979. Stress memory of crystalline rocks in acoustic emission, *Geophys. Res.,* **6**(1), 9–12.

Lavrov, A., 2001. Kaiser effect observation in brittle rock cyclically loaded with different loading rates, *Mech. Mater.,* **33**(11), 669–677.

Lavrov, A., 2003. The Kaiser effect in rocks: principles and stress estimation techniques, *Int. J. Rock Mech. Min. Sci.,* **40**(2), 151–171.

Li, C. & Nordlund, E., 1993. Experimental verification of the Kaiser effect in rocks, *Rock Mech. Rock Eng.,* **26**(4), 333–351.

Lockner, D.A., Byerlee, J.D., Kuksenko, V., Ponomarev, A. & Sidorin, A.,1992. Observations of quasistatic fault growth from acoustic

emissions, in *Fault Mechanics and Transport Properties of Rocks,* Vol. 51, pp. 3–31, eds Evans, B. & Wong, T., Academic Press, San Diego, Calif.

Lyakhovsky, V., Ben-Zion, Y. & Agnon, A, 1997. Distributed damage, faulting, and friction, *J. geophys. Res.,* **102**(B12), 27 635–27 649.

Lyakhovsky, V., Ben-Zion, Y. & Agnon, A., 2005. A viscoelastic damage rheology and rate- and state-dependent friction, *Geophys. J. Int.,* **161,** 179–190.

Lyakhovsky, V., Zhu, W. & Shalev, E., 2015. Visco-poroelastic damage model for brittle-ductile failure of porous rocks, *J. geophys. Res.,* **120**(4), 2179–2199.

Mair, K., Main, I. & Elphick, S., 2000. Sequential growth of deformation bands in the laboratory, *J. Struct. Geol.,* **22**(1), 25–42.

Malvern, L.E., 1969. *Introduction to the Mechanics of a Continuum Medium,* pp. 713, Prentice-Hall, Inc.

Marco, S., 2007. Temporal variation in the geometry of a strike–slip fault zone: examples from the Dead Sea Transform, *Tectonophysics,* **445**(3-4), 186–199.

Martyushev, L. & Seleznev, V., 2006. Maximum entropy production principle in physics, chemistry and biology, *Phys. Rep.,* **426,** 1–45.

Nair, A. & Cai, C.S., 2010. Acoustic emission monitoring of bridges: review and case studies, *Eng. Struct.,* **32**(6), 1704–1714.

Olsson, W.A. & Holcomb, D.J., 2000. Compaction localization in porous rock, *Geophys. Res.,* **27**(21), 3537–3540.

Onsager, L., 1931. Reciprocal relations in irreversible processes. *Phys. Rev.,* **37,** 405–416.

Panteleev, I., Lyakhovsky, V., Browning, J., Meredith, P.G., Healy, D. & Mitchell, T.M., 2020. Non-linear anisotropic damage rheology model: theory and experimental verification, *J. Mech. Phys. Solids,* submitted.

Pestman, B.J. & Van Munster, J.G., 1996. An acoustic emission study of damage development and stress-memory effects in sandstone, *Int. J. Rock Mech. Min. Sci. Geomech. Abstr.,* **33**(6), 585–593.

Prigogine, I., 1955. *Introduction to Thermodynamics of Irreversible Processes,* Springfield.

Rudnicki, J.W. & Rice, J.R., 1975. Conditions for the localization of deformation in pressure-sensitive dilatant materials, *J. Mech. Phys. Solids,* **23**(6), 371–394.

Sagar, R.V., Prasad, B.R. & Singh, R.K, 2015. Kaiser effect observation in reinforced concrete structures and its use for damage assessment, *Arch. Civ. Mech. Eng.,* **15**(2), 548–557.

Schultz, R.A. & Siddharthan, R., 2005. A general framework for the occurrence and faulting of deformation bands in porous granular rocks, *Tectonophysics,* **411**(1-4), 1–18.

Sedov, L.I., 1968. Variational methods of constructing models of continuous media, in *Irreversible Aspects of Continuum Mechanics and Transfer of Physical Characteristics in Moving Fluids,* eds Parkus, H. & Sedov, L.I., pp. 17–40, Springer-Verlag.

Shipton, Z.K. & Cowie, P.A., 2001. Damage zone and slip-surface evolution over μm to km scales in high-porosity Navajo sandstone, Utah, *J. Struct. Geol.,* **23**(12), 1825–1844.

Simpson, D.W. & Negmatullaev, S.K., 1981. Induced seismicity at Nurek reservoir, Tadjikistan, USSR, *Bull. seism. Soc. Am.,* **71**(5), 1561–1586.

Stefanov, Yu.P., Chertov, M.A., Aidagulov, G.R. & Myasnikov, A.V., 2011. Dynamics of inelastic deformation of porous rocks and formation of localized compaction zones studied by numerical modeling, *J. Mech. Phys. Solids,* **59**(11), 2323–2340.

Tembe, S., Vajdova, V., Baud, P., Zhu, W. & Wong, T., 2007. A new methodology to delineate the compactive yield cap of two porous sandstones under undrained condition, *Mech. Mater.,* **39**(5), 513–523.

Tengattini, A., Das, A., Nguyen, G.D, Viggiani, G., Hall, S.A. & Einav, I., 2014. A thermomechanical constitutive model for cemented granular materials with quantifiable internal variables. Part I—Theory, *J. Mech. Phys. Solids,* **70,** 281–296.

Truesdell, C. & Noll, W., 2004. *The Non-Linear Field Theories of Mechanics,* 3rd edn, pp. 627, ed. Antman, S.S., Springer-Verlag.

Tuncay, E. & Ulusay, R., 2008. Relation between Kaiser effect levels and pre-stresses applied in the laboratory, *Int. J. Rock Mech. Min. Sci.,* **45**(4), 524–537.

Vorobiev, O.Yu., Liu, B.T., Lomov, I.N. & Antoun, T.H., 2007. Simulation of penetration into porous geologic media, *Int. J. Impact Eng.,* **34**(4), 721–731.

Weinberger, R., Baer, G., Shamir, G. & Agnon, A., 1995. Deformation bands associated with dyke propagation in porous sandstone, Makhtesh Ramon, Israel, in *The Physics and Chemistry of Dykes,* eds Baer, G. & Heimann, A., pp. 95–112, Balkema.

Yoshikawa, S. & Mogi, K., 1981. A new method for estimation of the crustal stress from cored rock samples: laboratory study in the case of uniaxial compression, *Tectonophysics,* **74**(3-4), 323–339.

Zhang, M., Meng, Q., Liu, S., Qian, D. & Zhang, N., 2018. Impacts of cyclic loading and unloading rates on acoustic emission evolution and felicity effect of instable rock mass, *Adv. Mater. Sci. Eng.,* doi:10.1155/2018/8365396.

APPENDIX

To account for the coupled evolution of damage and porosity in poroelastic media, we generalize the results of Hamiel *et al.* (2004b) and Lyakhovsky *et al.* (2015) during irreversible brittle deformation. We follow the approach of irreversible thermodynamics (e.g. Onsager 1931; Biot 1955; Prigogine 1955; Truesdell & Noll 2004), which was successfully applied to kinetics of chemical reactions and phase transitions (e.g. de Groot & Mazur 1962; Fitts 1962) and served as a basis for variational methods of continuous media models (e.g. Sedov 1968; Malvern 1969; Berdichevsky 2009). The constitutive behaviour of the material and flow rules controlling the kinetics of related irreversible processes are entirely defined by the specification of two potentials: free energy and dissipation function or local entropy production. Using the balance equations of the energy and entropy, Gibbs relation, fluid mass conservation equation, the definitions of the stress tensor, and fluid pressure, Hamiel *et al.* (2004b) derived the local entropy production, Γ, related to the kinetics of porosity, ϕ, and damage, α:

$$\Gamma = -\frac{\partial F}{\partial \alpha}\frac{\mathrm{d}\alpha}{\mathrm{d}t} - P_\mathrm{e}\frac{\mathrm{d}\phi}{\mathrm{d}t}, \tag{A1}$$

where P_e is the effective pressure or mean stress minus fluid pressure, and F is the free energy. Onsager (1931) theoretically generalized the empirical laws of Fourier, Ohm, Fick and Navier, representing the specific local entropy production as a product of thermodynamic fluxes and thermodynamic forces and adopting linear relations between them (see review by Martyushev & Seleznev 2006). Following the Onsager principle, Hamiel *et al.* (2004b) and Lyakhovsky *et al.* (2015) formulated the kinetic relations for damage and porosity evolution as a system of equation:

$$\frac{\mathrm{d}\phi}{\mathrm{d}t} = -C_{\phi\phi}\,P_\mathrm{e} - C_{\phi\alpha}\frac{\partial F}{\partial \alpha} \tag{A2}$$

$$\frac{\mathrm{d}\alpha}{\mathrm{d}t} = -C_{\alpha\phi}P_\mathrm{e} - C_{\alpha\alpha}\frac{\partial F}{\partial \alpha}, \tag{A3}$$

where $C_{\alpha\alpha}$, $C_{\phi\phi}$, $C_{\alpha\phi}$, $C_{\phi\alpha}$ are kinetic coefficients or functions of the state variables. The diagonal terms, first in (A2) and second in (A3) are responsible for the evolution of α and ϕ as functions of damage and porosity related forces, while the other terms are responsible for the coupling between the kinetics of damage and porosity. Hamiel *et al.* (2004b) suggested that $C_{\alpha\phi}$ is a power-law expression of the effective pressure, $C_{\alpha\phi} \sim P_\mathrm{e}{}^n$. They demonstrated that the transition from positive to negative values of the slope of the yield curve (yield cap) is a general feature of the model. With this form of the kinetic coefficient, their model defines the yielding condition in stress-space as being a function of the effective

pressure. Their formulation actually mixed stress–space and strain–space formulation for the kinetics of damage. Lyakhovsky *et al.* (2015) fixed this shortcoming formulation converting stress into strain–space relations (see their eq. 14):

$$\frac{\mathrm{d}\alpha}{\mathrm{d}t} = C_{\mathrm{d}}\left[D\left(\alpha,\varphi\right)\left(-I_1\right)^{n+2} + I_2\left(\xi - \xi_0\right)\right] \tag{A4}$$

where $I_1 = \epsilon_{kk}$, $I_2 = \epsilon_{ij}\ \epsilon_{ij}$ are invariants of the strain tensor; $\xi = I_1/\sqrt{I_2}$ is the strain invariant ratio and its critical value $\xi = \xi_0$ controlling dilation-compaction transition. The derivative $\partial F/\partial\alpha \sim -I_2(\xi - \xi_0)$ gives the second term in (A4) increasing with strain in power two while coupling the term with $C_{\alpha\phi} \sim (-I_1)^{n+1}$ with $n > 0$ increases with strain in a higher power and becomes dominant at elevated strain values. The competition between these terms leads to the damage increase even below the dilation-compaction transition at $\xi = \xi_0$ (see Lyakhovsky *et al.* 2015 for details). In such a regime, with $\xi < \xi_0$, the damage-related term in (A1) is negative, which seems to violate the non-negative dissipation. However, even small compaction ($\mathrm{d}\phi/\mathrm{d}t < 0$) fixes this problem. All or part of the energy release due to porosity decrease is transferred into the energy needed for fracturing, providing positive dissipation. When the loading conditions overcome the dilation-compaction condition ($\xi > \xi_0$), the damage related dissipation becomes positive, and the energy goes into dilation. In this study, we are focused only on the details of the damage growth without going into details of the porosity change. For the drained conditions or dry rocks with constant or zero fluid pressure, it does not affect the stress-strain relations and could be excluded from the consideration. For the 1-D problem considered in this study addressing uniaxial compression, the strain invariants are $I_1 = -\sqrt{I_2} = \varepsilon(x,t)$ and the strain invariant ratio is $\xi = -1$, which is below typical ξ_0-values estimated by Lyakhovsky *et al.* (1997) from the internal friction angle. Substituting these values into (A4) leads to the simplified equation of the damage evolution:

$$\frac{\mathrm{d}\alpha}{\mathrm{d}t} = C_{\mathrm{d}}\left[D\left(\alpha,\varphi\right)\varepsilon^{n+2} + \varepsilon^2\left(1 - \xi_0\right)\right]. \tag{A5}$$